



ISTITUTO NAZIONALE DI RICERCA METROLOGICA
Repository Istituzionale

Composite Raman-Nath heterodyne interferometry with relevance for precise spectroscopy

Original

Composite Raman-Nath heterodyne interferometry with relevance for precise spectroscopy / Barbiero, M., Salvatierra, J.P., Calonico, D., Levi, F., Tarallo, M.G.. - In: OPTICS AND LASER TECHNOLOGY. - ISSN 0030-3992. - 181:(2025). [10.1016/j.optlastec.2024.111613]

Availability:

This version is available at: 11696/81499 since: 2024-09-27T08:12:45Z

Publisher:

Elsevier

Published

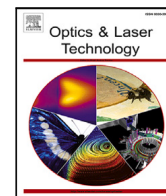
DOI:10.1016/j.optlastec.2024.111613

Terms of use:

This article is made available under terms and conditions as specified in the corresponding bibliographic description in the repository

Publisher copyright

(Article begins on next page)



Full length article

Composite Raman-Nath heterodyne interferometry with relevance for precise spectroscopy

Matteo Barbiero ^{a,*}, Juan Pablo Salvatierra ^{a,b}, Davide Calonico ^a, Filippo Levi ^a, Marco G. Tarallo ^a

^a Istituto Nazionale di Ricerca Metrologica, Strada delle Cacce 91, Torino, 10134, Italy

^b Politecnico di Torino, Dipartimento di Elettronica e Telecomunicazioni, Corso Duca degli Abruzzi 24, Torino, 10129, Italy

ARTICLE INFO

Keywords:

Optical metrology
Raman-Nath diffraction
Frequency standards
Phase noise

ABSTRACT

Atomic state manipulation by laser radiation requires a stringent control of the light phase noise for precise spectroscopy and quantum computation. In this work we describe a novel interferometer recently employed to estimate the phase noise induced by an optical frequency shifter based on serrrodyne modulation for optical frequency standards (Barbiero et al., 2023). The interferometer is generated by an acousto-optic actuator working in the Raman-Nath regime. Using the heterodyne detection between the unshifted optical mode with the first higher order optical components, we are able to detect the differential phase between the two optical path arms with a reduction of the phase noise induced by the actuator. We provide a theoretical treatment for the actuator phase suppression and we estimate the detectable phase noise limit of this interferometer. Finally, we discuss the possible applications in the field of precision measurements.

1. Introduction

The ever-increasing demand for precision control of the internal state of quantum systems, such as neutral atoms [1,2], ions [3] and molecules [4] for quantum computing, quantum simulation [5,6], and quantum metrology [7,8] requires ultralow noise, highly spectrally pure, and highly stable optical oscillators. The control and tuning of the oscillators optical phase also demands stringent constraints on their photonic devices to avoid incoherent (spurious) spin flips during manipulation of optical qubits and laser-driven gates [9,10]. As the quality of the optical oscillator improves, the need for phase noise measurement systems capable of precisely characterizing them has also grown.

Optical heterodyne and homodyne interferometry are powerful optical techniques used to achieve high sensitivity measurement of small phase shifts. Contrary to the optical homodyne method, heterodyne interferometry measures the beatnote between two different optical frequencies where the desired phase information is encoded in one of the two optical frequencies. As long as a perfect coherence is assumed and a classical treatment of the electromagnetic field is applied, the maximum signal-to-noise ratio (SNR) achieved by heterodyne interferometry is a factor of $\sqrt{2}$ lower than the homodyne counterpart [11]. On the other hand, the heterodyne interferometer reaches its maximum SNR without a mandatory stabilization of the reference optical path as in the case of the homodyne one [11]. This versatility of the heterodyne

method is also confirmed in the full quantum treatment of the electromagnetic field [12]. Successful applications of the optical heterodyne interferometry are numerous, such as solar radiometry [13], coherent Doppler laser ranging application [14], frequency modulation spectroscopy [15], cavity ring down spectroscopy [16] and measurement of laser phase noise [17].

In a recently published work [18] a new composite heterodyne interferometer has been proposed and utilized, which merges multipath optical interferometry [19] with the heterodyne phase measurement technique. The multiple beams of this interferometer are generated by an acousto-optic modulator (AOM) operating in the Raman-Nath (RN) regime. The primary feature of RN diffraction is the spatial separation of diffracted orders where each of them have a defined phase modulation. This configuration can be easily optically generated by passing a laser beam through an AOM aligned to avoid resonant Bragg diffraction. Examples of interferometric schemes involving the RN diffraction regime include the frequency-modulation spectroscopy in Coherent-Population-Trapping resonances [20,21] and a real-time minimally destructive probing method of atoms in an optical lattice [22].

In this work, we describe the composite Raman-Nath interferometer (CRNI) generated by a laser beam diffracted by a AOM operating in the RN regime from which two parallel Mach-Zehnder interferometers (MZIs) are inferred and an heterodyne phase measurement is extracted [18]. This proposed interferometer is similar to a double Mach-Zehnder heterodyne interferometer where one branch of

* Corresponding author.

E-mail address: m.barbiero@inrim.it (M. Barbiero).

<https://doi.org/10.1016/j.optlastec.2024.111613>

Received 5 March 2024; Received in revised form 8 August 2024; Accepted 12 August 2024

Available online 29 August 2024

0030-3992/© 2024 The Authors. Published by Elsevier Ltd. This is an open access article under the CC BY license (<http://creativecommons.org/licenses/by/4.0/>).

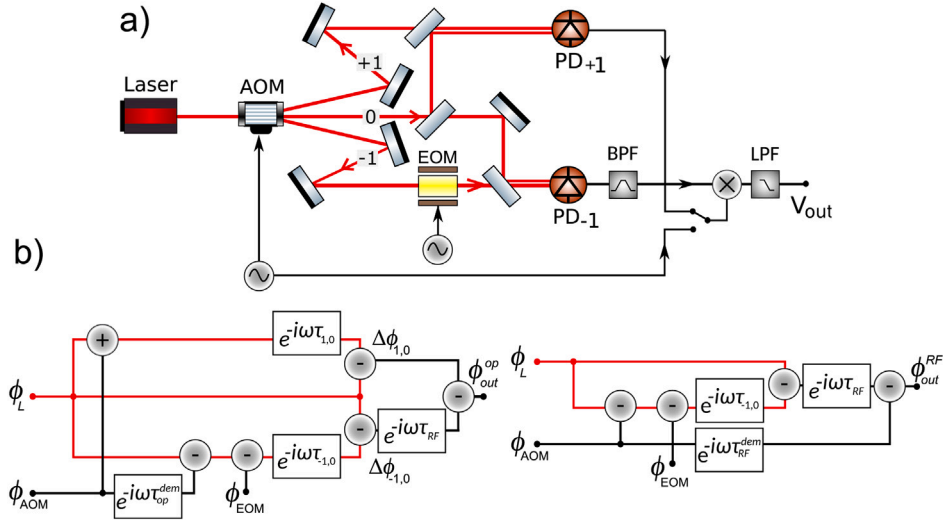


Fig. 1. Illustration of the experimental realization and the conceptual phase analysis of a CRNI. (a) Schematic drawing of the experimental setup including all the essential optical and electronic elements. $PD_{\pm 1}$: photodetectors; BPF: band-pass filter; LPF: low-pass filter; AOM: acousto-optic modulator; EOM: electro-optic modulator; V_{out} : output voltage signal. (b) Delay line theoretical model in the Fourier domain ($\omega = 2\pi f$). The left panel depicts the optical demodulation process induced by the CRNI while the right panel shows the standard RF demodulation process. The red lines represent the optical domain while the black lines are the RF domain. The phases ϕ_i and the delays τ_i imprinted on the laser optical phase ϕ_L are described in the main text.

the interferometer is frequency shifted: after a proper signals manipulation, the RN actuator phase noise is expected to be greatly suppressed. Similar interferometers that exploit a double heterodyne detection were already employed to suppress common source of noise in precision spectroscopy measurements [23,24]. We investigate the performance of this heterodyne interferometer based on optical demodulation process in detail, and we compare its performance with a common interferometer scheme which exploits the Radio-Frequency (RF) demodulation.

The article is organized as follows: in Section 2 we describe the phase sensitivity and the expected phase noise sources in a CRNI. In Section 3 we report the details of our experimental realization of a CRNI apparatus. Finally in Section 4 we present the main results of our investigation.

2. Composite Raman-Nath heterodyne interferometry theory

The CRNI consists of two Mach-Zehnder interferometers (MZIs) generated by a laser beam impinging on the AOM, where the common reference arm is the unshifted AOM's zeroth diffraction order, while the +1 and -1 diffraction orders yield two separate MZIs' beatnote frequencies for heterodyne phase detection. In the example depicted in Fig. 1(a), the diffracted order -1 is phase modulated by an electro-optic modulator (EOM), which works as device under test. The two optical ports of the CRNI are then detected by two photodetectors, namely $PD_{\pm 1}$ where the sign refers to the diffraction order related CRNI branch. Two RF signals are then generated, $V_{PD_{\pm 1}}$. After proper filtering, the generated optical beatnotes are mixed in order to remove the phase induced by the AOM, and then to extrapolate the phase noise information provided by the actuator under test.

2.1. CRNI phase signal extraction

The left panel of Fig. 1(b) reports the physical model of the CRNI using delay-line theory [25]. The beatnotes acquired from the photodiodes can be written as $V_{PD_{-1}} = V_{-1} \cos(\Delta\phi_{-1,0})$ and $V_{PD_{+1}} = V_{+1} \cos(\Delta\phi_{+1,0})$ where $\Delta\phi_{i,0}$ is the relative phase difference measured by a single MZI, including the RF heterodyne frequency and all its time dependence. At the detection time t , the beatnotes acquired from the photodiodes PD_{-1} and PD_{+1} can be written as:

$$\Delta\phi_{1,0}(t) = \phi_{AOM}(t) + [\phi_L(t) - \phi_L(t - \tau_{1,0})] + k_L \Delta l_{1,0} \quad (1)$$

$$\Delta\phi_{-1,0}(t) = \phi_G(t) + \phi_{AOM}(t) + [\phi_L(t) - \phi_L(t - \tau_{-1,0})] + k_L \Delta l_{-1,0} \quad (2)$$

where $\phi_{AOM}(t)$ and $\phi_L(t)$ are the phase acquired from the AOM diffraction and the laser phase, respectively. The generic dephasings $k_L \Delta l_{i,0}$ and the delay times $\tau_{i,0} = \Delta l_{i,0}/c$ arise from the optical paths unbalance of the MZIs. Finally, the $\phi_G(t)$ is the phase acquired from the device under test which includes the frequency shift of the optical carrier necessary for heterodyne interferometry. After mixing the beatnotes acquired from $PD_{\pm 1}$, the CRNI output signal can be written as $V_{out} = k_\phi \sqrt{V_{-1} V_{+1}} \cos(\phi_{out}^{op})$ where k_ϕ is the mixer conversion factor and $\phi_{out}^{op} = \Delta\phi_{-1,0}(t) - \Delta\phi_{+1,0}(t)$ is the expected phase from the optical demodulation computed as follow:

$$\phi_{out}^{op}(t) = \phi_G(t) + [\phi_{AOM}(t) - \phi_{AOM}(t - \tau_{op}^{dem})] + [\phi_L(t) - \phi_L(t - \tau_{RN})] + k_L \Delta l_{RN} \quad (3)$$

where $\Delta l_{RN} = (\Delta l_{-1,0} - \Delta l_{+1,0})$, $\tau_{RN} = \Delta l_{RN}/c$, and τ_{op}^{dem} is a generic delay time arising between the optical diffraction orders generated from the AOM in the RN configuration.

We compare this optical demodulation with RF demodulation which is the most widespread strategy to extract phase information. The physical model of RF demodulation is reported in the right panel of Fig. 1(b). In this scheme, the optical beatnote measured by the photodiode PD_{-1} is mixed with the RF signal generated by the AOM Local Oscillator (LO) to cancel its phase noise contribution. The acquired phase $\Delta\phi_{-1,0}(t)$ is mixed with the $\phi_{AOM}(t - \tau_{RF}^{dem})$ generated by the AOM LO. Also in this case we consider a delay time τ_{RF}^{dem} to take into account the possible delay line between the acquired signal from PD_{-1} and the AOM LO. The extracted heterodyne phase ϕ_{out}^{RF} is the following:

$$\phi_{out}^{RF}(t) = \phi_G(t) + [\phi_{AOM}(t) - \phi_{AOM}(t - \tau_{RF}^{dem})] + [\phi_L(t) - \phi_L(t - \tau_{-1,0})] + k_L \Delta l_{-1,0} \quad (4)$$

Switching to the Fourier domain, Eqs. (4) and (3) can be re-written as:

$$\begin{aligned} \tilde{\phi}_{out}^{op}(f) &= \tilde{\phi}_G(f) + H(\Delta\varphi_{op}^{dem}) \cdot \tilde{\phi}_{AOM}(f) + H(\Delta\varphi_{RN}) \cdot \tilde{\phi}_L(f) \\ &\quad + k_L \tilde{\Delta} l_{RN}(f) \\ \tilde{\phi}_{out}^{RF}(f) &= \tilde{\phi}_G(f) + H(\Delta\varphi_{RF}^{dem}) \cdot \tilde{\phi}_{AOM}(f) + H(\Delta\varphi_{-1,0}) \cdot \tilde{\phi}_L(f) \end{aligned} \quad (5)$$

$$+ k_L \tilde{\Delta L}_{-1,0}(f) \quad (6)$$

where $\Delta\varphi_{-1,0} = 2\pi f \tau_{-1,0}$ and $\Delta\varphi_{RN} = 2\pi f \tau_{RN}$ are the dephasing generated by their optical delay line while the $\Delta\varphi_{RF}^{dem}$ and $\Delta\varphi_{op}^{dem}$ are the dephasing arising between the different delay time associated to the different demodulation scheme. In Eqs. (6) and (5) we have introduced $H(\Delta\varphi) = (1 - e^{i\Delta\varphi})$, which is the delay line transfer function.

2.2. Analysis of CRNI phase noise

The associated phase noise power spectral densities of the two extracted phases in Eqs. (5) and (6) can be estimated as:

$$S_{out}^{op} = S_G + |H(\Delta\varphi_{op}^{dem})|^2 S_{AOM} + |H(\Delta\varphi_{RN})|^2 S_L + 2S_{env} + 2S_{det} \quad (7)$$

$$S_{out}^{RF} = S_G + |H(\Delta\varphi_{RF}^{dem})|^2 S_{AOM} + |H(\Delta\varphi_{-1,0})|^2 S_L + S_{env} + S_{det} \quad (8)$$

where S_G is the phase noise of the actuator under test, S_{AOM} is the phase noise of the AOM LO, S_L is the phase noise of the laser, $|H(\Delta\varphi)|^2 = 4 \sin^2(\Delta\varphi/2)$, S_{env} is the phase noise induced by the optical path fluctuation $k_L \Delta l$ and S_{det} is the phase-noise induced by the optical detection. In the Eq. (7), a factor of 2 in the S_{env} and S_{det} is introduced compared to the Eq. (8) considering the presence of two identical photodetectors and assuming uncorrelated phase noises induced by the optical paths fluctuations $\Delta l_{-1,0}$ and $\Delta l_{1,0}$. The term S_G in both Eqs. (7) and (8) is related to the actuator phase noise that the interferometer aims to unravel. All the other noise sources are associated with the applied interferometric scheme, which limits our signal to noise ratio.

Following Eqs. (7) and (8), we can analyze some of the phase noise limits affecting the extracted phases ϕ_{out}^{op} and ϕ_{out}^{RF} . Except for unknown values of S_{env} , $\Delta\varphi_{RF}^{dem}$ and $\Delta\varphi_{op}^{dem}$, all the other contributions can be measured or estimated a priori. The laser phase noise S_L and the AOM actuator phase noise S_{AOM} are weighted by their delay line transfer functions. If the delay times $\tau_{-1,0}$, τ_{RN} are higher than the coherence time of the laser, the laser phase fluctuation cannot be completely neglected. The same is valid for the AOM phase noise cancellation: the different delay times τ_{op}^{dem} and τ_{RF}^{dem} induced by the different demodulation strategies may reduce or increase the weight of the AOM phase noise in the final phase extraction.

The detection process is also affected by a fundamental limit provided by the photon shot-noise and by thermal-noise affecting the electronic components. This noise is estimated according the following formula [25]:

$$S_{det} = \frac{16}{m^2} \left[\frac{h\nu}{\eta} \frac{1}{P} + \left(\frac{F k_B T}{Z_L} \frac{h\nu}{e\eta} \right)^2 \frac{1}{P^2} \right] \quad (9)$$

where m is the power modulation index defined as $m = 2\sqrt{P_{\pm 1} P_0}/P$ and $P = P_0 + P_{\pm 1}$ is the total optical power impinging on the photodiode $PD_{\pm 1}$ while P_0 and $P_{\pm 1}$ are the optical power of the 0 and ± 1 -orders, F is the noise figure from the built-in amplifier of the photodiode, η is the quantum efficiency, ν is the photon frequency, h is the Plank constant, e is the electron charge, k_B is the Boltzmann constant, T is the temperature and Z_L is the load's impedance (which is typically 50 Ω). In Eq. (9), the term $1/P$ is due to photodiode shot-noise while the term $1/P^2$ is due to thermal-noise induced by built-in amplifier in the photodiode.

2.3. Light diffraction regime by ultrasonic field

The core of the CRNI is the diffraction pattern generated by the AOM. It is well known that the geometrical properties of the diffraction of an optical beam from an ultrasonic field propagating in a crystalline medium (the AOM) can be described by the Klein-Cook parameter Q [26]. This parameter is defined as $Q = 2\pi L \lambda / n_0 \Lambda^2$ where λ is the optical wavelength, Λ is the ultrasound wavelength inside the crystal, n_0 is the refraction index of the acousto-optic crystal and L is the interaction length between the laser and ultrasonic field. Three

different diffraction regimes are identified according to the value of Q : the Bragg regime ($Q \gg 1$), the pure Raman-Nath regime ($Q \ll 1$) and the transition regime ($Q \simeq 1$). The resulting diffraction pattern for the case of the pure RN regime ($Q \ll 1$) and the Bragg regime can be solved analytically [26]. In the former case, the expected first order diffracted light power $P_{\pm 1}$ is estimated to be [26,27]:

$$P_{\pm 1} = P_L J_1^2(\beta) \quad (10)$$

where P_L is the impinging optical power to the AOM, J_1 is the first order Bessel function of the first kind and β is the modulation index, defined as [27]:

$$\beta = 2\pi \frac{L}{\lambda} \Delta n, \quad \Delta n = \sqrt{\frac{M_2 I_s}{2}} \quad (11)$$

where Δn is the variation of the refractive index due to the ultrasound field, $M_2 = n_0^6 p^2 / \rho v_s^3$ is a figure of merit of the crystal, where p is the dimensionless effective elasto-optic constant which describes the change of the refractive index of the optical medium due to the presence of the acoustic wave, ρ is the crystal density, v_s is the sound speed in the crystalline medium, and I_s is the ultrasound intensity. The crystal birefringence, the residual amplitude modulation, and phonon-phonon scattering are not considered in this work [28,29]. Nevertheless, they were demonstrated to play a marginal role if a proper design of the AOM in the RN regime are adopted [30].

3. Experimental apparatus

The experimental setup is depicted in Fig. 1(a). Our laser source is a commercial external cavity diode laser (Toptica, DL pro) working at 698 nm referenced to a 10 cm long ultra-stable ULE cavity. The details of the laser frequency stabilization system can be found elsewhere [18]. Almost 3.7 mW of laser radiation with beam diameter of $w = 1.2(2)$ mm is sent to a commercial AOM made by TeO₂ crystal (Gooch & Housego, 3080-122). The AOM is driven by a local oscillator (Siglent, SDG2122X) generating a sinusoidal frequency at 80 MHz. The signal is properly amplified to reach a RF power of 30 dBm generating almost 1 mW in both diffraction orders at +80 MHz and -80 MHz from the optical carrier ν . Following the optical path shown in Fig. 1(a), the +1 diffraction order is then recombined with the 0 order of the AOM and impinges on the photodiode PD_{+1} . The -1 diffraction order passes through a free space EOM (Thorlabs, EO-PM-R-10-C1) and then is recombined with the 0 order at the photodiode PD_{-1} . A free space EOM is employed as frequency shifter and device under test. A low phase noise local oscillator (Agilent, 33255 A) is used to drive the EOM at 10 MHz and the first order sidebands are maximized injecting 23 dBm of RF power. We ensure that almost the same optical power $P = 0.8(1)$ mW impinges on both photodiodes PD_{-1} and PD_{+1} . The amplified photodiodes employed in our apparatus are identical (Newport, 818-BB-21 A) and they are characterized by a broad detection bandwidth of 2 GHz, conversion gain of $\mathcal{G} = 0.5$ V/mW and responsivity of $\mathcal{R} = 0.475$ A/W which provides a quantum efficiency of $\eta = \mathcal{R} h\nu / e = 0.80$ at $\nu = 429$ THz. The readout signals from the photodiodes exceed 60 dB of SNR at 100 kHz of resolution bandwidth. The output of PD_{-1} passes through a narrow and tunable high order Band-Pass Filter (BPF) (Telonic, TTF-95-5-5-EE) centered at 70 MHz with a measured power bandwidth of 5.6(2) MHz. Finally, the filtered signal is then demodulated directly by the LO used to drive the AOM or by the optical beatnote acquired from the photodiode PD_{-1} . The demodulated signal is then low-pass filtered (Minicircuits, SPL-10.7+), amplified and measured with a low noise phasemeter (Microsemi, 5125 A), whose phase noise floor is lower than 1×10^{-16} rad²/Hz above 1 kHz. The reference signal of the phasemeter is provided by a 10 MHz generated by an H-maser used for the realization of the UTC(IT) timescale. The extra phase noise induced by our phase sensitive detector (Minicircuits, ZFM-3-S+) [31] and the RF amplifier (Minicircuits, ZHL-500LN+) [32] are below 1×10^{-17} rad²/Hz at an offset frequency of 100 kHz which is lower than the phase noise floor of our phasemeter.

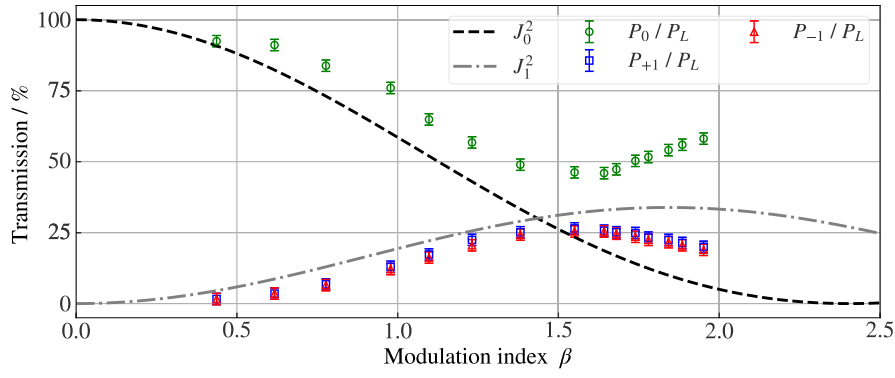


Fig. 2. Transmission of the first AOM diffracted orders as a function of the estimated modulation index β . The green circles, the blue squares, and the red triangles report the transmission of the 0th, +1st, and -1st AOM orders, respectively. The black and the gray lines are the square of the Bessel functions $J_0^2(\beta)$ and $J_1^2(\beta)$, respectively.

4. Results

4.1. Raman-Nath light diffraction characterization

The diffraction regime of the AOM to operate a CRNI is obtained by carefully tuning the AOM alignment with respect to the input optical beam in order to generate the same optical power in the first orders of diffraction -1 and $+1$. The estimated Klein–Cook parameter for our experiment is $Q^{\text{est.}} = 2\pi L\lambda/(n_0\Lambda^2) = 6.7(7)$ where $n_0 = 2.367$ is the refractive index of TeO_2 , $\lambda = 698\text{ nm}$ is the optical wavelength, $\Lambda = 52.2\ \mu\text{m}$ is the ultrasound wavelength traveling inside the crystal and $L = 10(1)\text{ mm}$ is the estimated laser-ultrasound interaction region. The estimated value of L is set to be roughly the width of the transducer [26]. The value of $Q^{\text{est.}}$ suggest us that our AOM is not able to reach a pure Raman-Nath regime which is also reasonable because the AOM employed in this work is designed to work in the Bragg condition maximizing the transmission intensity of one specific diffraction order. A lower frequency modulation or a thinner Bragg cell with a shorter interaction region L are usually employed achieve the pure Raman-Nath regime [21].

The intermediate regime is also evinced by analyzing the intensity of the diffracted order as a function of the modulation index β . Fig. 2 reports the efficiency of the first diffraction orders as a function of the estimated modulation index β computed according to Eq. (11). We measured the transmission of the un-diffracted order (green points) and the first orders of AOM diffraction (blue and red points) while the black and the gray curve are the square of the Bessel functions J_0^2 and J_1^2 , respectively, predicted for a pure RN regime ($Q \ll 1$).

Considering negligible insertion losses ($<3\%$), we estimate the sound intensity injected to the crystal as $I_s = P_{\text{RF}}/(Lh)$, where P_{RF} is the RF power sent to the AOM, $h = 1.0(2)\text{ mm}$ is the width of the acoustic-optic interaction region, and $L = 10(1)\text{ mm}$ is the usual interaction length. In the case of commercially available AOMs based on TeO_2 crystals, the figure of merit is $M_2 = 3.46e-14\ \text{s}^3\ \text{kg}^{-1}$ for a linear optical polarization [27]. It is clear that the measured transmission of the first diffracted orders do not match with the expected trends for a phase modulation represented with the Bessel functions. In particular, there is no modulation index such that the un-diffracted beam intensity drops to zero, as expected for the Bessel function J_0^2 . We observe the same diffraction efficiency for different beam diameters. Comparing our experimental characterization with the numerical simulations reported in [26], we believe that we achieved a transition regime $4 < Q < 7$ which confirm our prior estimation of $Q^{\text{est.}} = 6.7(7)$.

4.2. Sources of noise in the interferometer

We now describe in detail the performances of our prototype of CRNI, starting from the contributing noise sources, as analytically described by Eqs. (7) and (8). Fig. 3 reports the noise sources affecting

our interferometer as measured independently from our CRNI setup. In this work, a low phase noise LO is used to drive the phase actuator under test. This low noise LO is selected on purpose in order to evince the role of different demodulation schemes used to extrapolate the signals $\phi_{\text{out}}^{\text{RF}}$ and $\phi_{\text{out}}^{\text{op}}$.

The first noise source to be considered is the AOM, in particular the phase noise imprinted by its driving LO. The AOM LO phase noise (blue line in Fig. 3) shows almost a white noise spectrum of $S_{\text{AOM}} \approx 3.0 \times 10^{-11}\ \text{rad}^2/\text{Hz}$ in the frequency region of 1 kHz to 1 MHz. It contributes to the phase noise of the interferometer by means of the delay line transfer function H of the RF setup. The phase noise induced solely by the electronic RF delay line is estimated by mimicking the signals acquired from photodiodes before the demodulation. We split the RF signal generated from the AOM LO: one RF component is sent directly to the reference channel of the phasemeter, while the other RF component is first sent to the narrow band-pass filter and then connected to the input channel of the phasemeter. The red line in Fig. 3 shows the phase noise acquired from the aforementioned setup. The squared RF transfer function $|H(\Delta\phi_{\text{RF}})|^2$ is obtained by dividing the measured RF delay line phase noise (red curve) with the input AOM LO phase noise (blue curve). At frequencies higher than 1 kHz, we found that the RF dephasing evolves according to:

$$\Delta\phi_{\text{RF}}(f) = \arctan(f/f_1) + \arctan(f^2/f_2^2) \quad (12)$$

where $f_1 = 0.812(3)\text{ MHz}$ and $f_2 = 1.188(3)\text{ MHz}$ are the fit result frequencies. The use of high-order arctan functions in Eq. (12) takes into account potential a highly non-linear dephasing response of the RF system. The resulting RF delay time is $\tau_{\text{RF}} = (2\pi f_1)^{-1} = 196.0(8)\text{ ns}$, mainly limited by the BPF dephasing and other electronic sources of delay. The orange curve in Fig. 3 reports the reconstructed RF delay line obtained multiplying the input phase noise of the AOM LO with the squared of the extrapolated RF delay line transfer function $|H(\Delta\phi_{\text{RF}})|^2$.

We also consider the laser phase noise contribution as a possible noise source of the interferometer. Once referred to the 10 cm ULE cavity, the laser phase noise is estimated as $S_L \sim af^{-3} + bf^{-1} + c$ where $a = 2\ \text{rad}^2\ \text{Hz}^2$, $b = 5.2e-2\ \text{rad}^2\ \text{Hz}$ and $c = 1.6 \times 10^{-8}\ \text{rad}^2/\text{Hz}$ [33]. As reported in Eqs. (8) and (7), the laser phase noise is transferred to the output signal by means of H once an optical path imbalance is introduced. In our setup, both arms of the CRNI have an optical path imbalance below $\Delta l \approx 20\text{ cm}$ in both interferometers, so that $\Delta l_{-1,0} = \Delta l_{\text{RN}} = \Delta l$. This optical path imbalance generates an optical delay time of $\tau_{\text{op}} \approx 0.66\text{ ns}$ which provides a linear dephasing $\Delta\phi(f) = 2\pi f\tau_{\text{op}}$. The contributions of the laser phase referred to the ULE cavity is reported as the brown dashed line in Fig. 3. We can appreciate that the frequency-stabilized laser used in this work generates a negligible noise source for the interferometer.

We also estimate a $S_{\text{det}} = 4.5(10) \times 10^{-14}\ \text{rad}^2/\text{Hz}$ for single photodiode setting $F = 3\text{ dB}$, $T = 300\text{ K}$, $P = 0.8(1)\text{ mW}$ and $m = 0.93$. The S_{det}

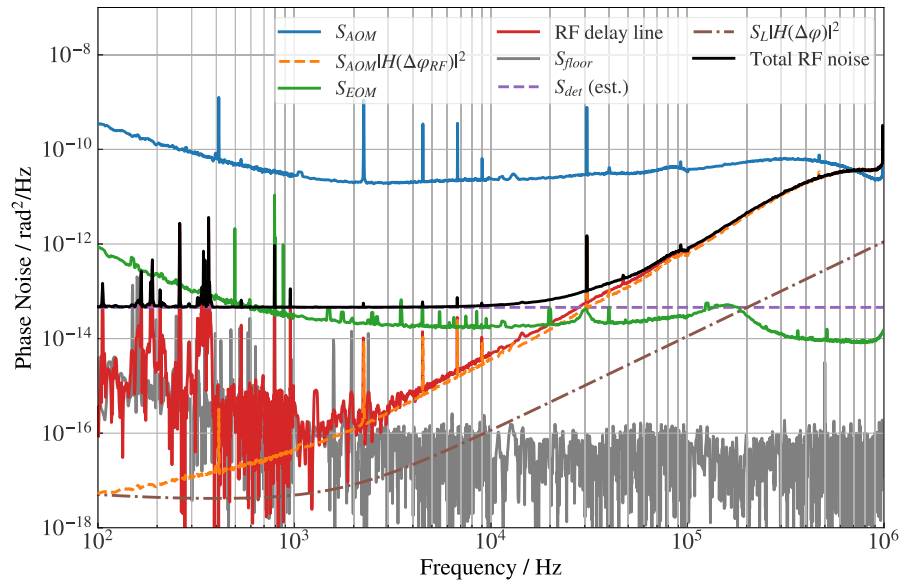


Fig. 3. Interferometer noise sources. The blue and green curves are the phase noises of the LOs used to drive the AOM and the EOM. The red curve is the measured phase noise increment due to the uncompensated RF line while the orange curve is its predicted noise. The dashed purple line is the estimated white phase noise due to the photodiode. The brown dashed line is the laser phase noise contribution arising from an optical path imbalance of 20cm. The black curve is the overall RF noise of the interferometer. The grey line is the measurement noise floor from the phasemeter.

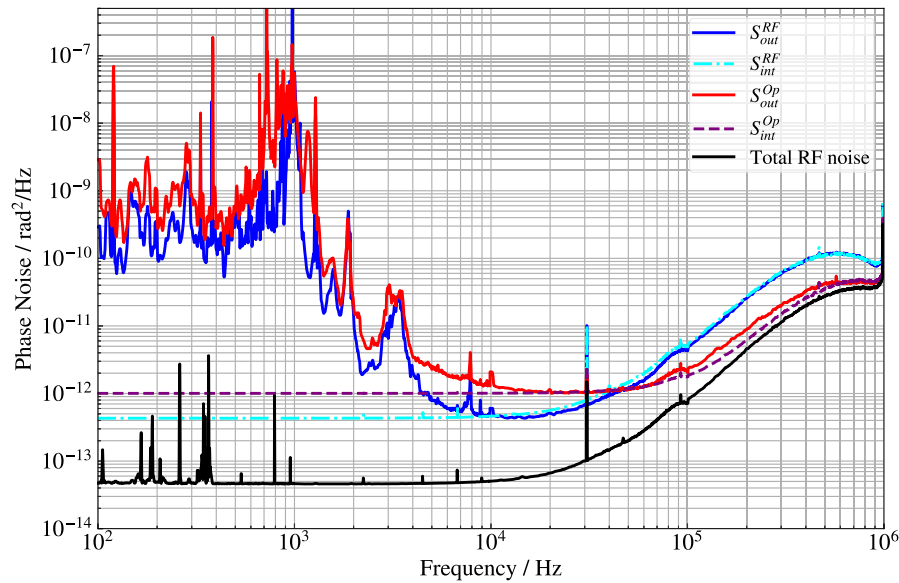


Fig. 4. Phase noise power spectral densities in a CRNI. The red curve is the phase noise extracted from the optical demodulation. The blue curve is the phase noise extracted by means of RF demodulation. The cyan and purple dashed line are the model noise for the two interferometers at frequencies higher than 10kHz (see main text for details). The black line is the noise of the interferometer from Fig. 3.

is reported in Fig. 3 as dashed purple line, and should be the dominant noise source between 1 kHz and 20 kHz.

Finally, the black line of Fig. 3 is the RF noise budget of our interferometer considering the above discussed technical noises. We can see that at Fourier frequencies between 1 kHz and 20 kHz we expect to be limited by the detection noise, while at frequencies higher than 20 kHz we are limited by the RF delay line that couples back the phase noise of the LO used for the demodulation.

The green curve reports the phase noise of the actuator under test which is well described by a white noise $S_{EOM} \approx 2.0 \times 10^{-14} \text{ rad}^2/\text{Hz}$ at frequency higher than 1 kHz. Unlike [18], a free space EOM is employed to reduce the high level of phase noise generated by the fiber coupled EOM.

4.3. Interferometer performances

We finally measure the phase noise levels in a CRNI by comparing the two demodulation strategies described so far, i.e. the optical demodulation vs. the RF demodulation scheme. In Fig. 4 the red curve shows the measured interferometer phase noise S_{out}^{Op} obtained by the optical demodulation, while the blue curve reports the measured interferometer phase noise provided by the RF demodulation S_{out}^{RF} . Both spectra are dominated by acoustic and seismic noise S_{env} in the frequency region below 1 kHz while at higher Fourier frequencies they seem to be limited by a frequency dependent dephasing caused by the employed different interferometric schemes, as described by Eqs. (7) and (8). By adding the previously characterized RF delay $\Delta\varphi_{RF}$, we can

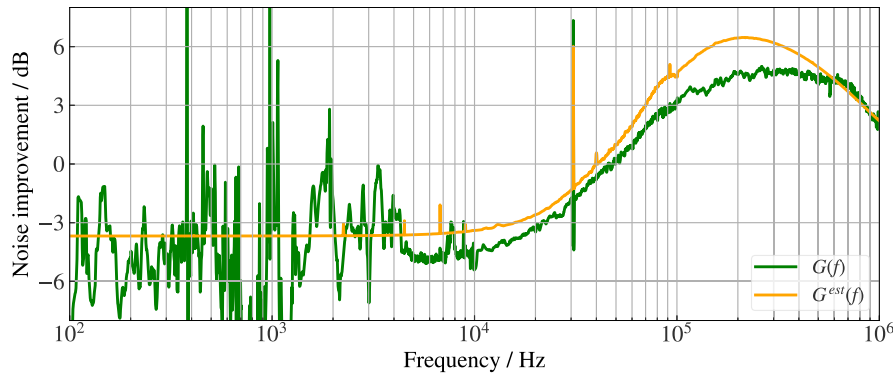


Fig. 5. Noise improvement provided by the CRNI. The green and the orange curve report G and G^{est} , respectively.

modify these expressions and fit our data at frequencies higher than 10 kHz with the following phase noise models:

$$S_{int}^{op} = S_0^{op} + |H(\Delta\varphi_{RF} + \Delta\varphi_{op}^{dem})|^2 S_{AOM} \quad (13)$$

$$S_{int}^{RF} = S_0^{RF} + |H(\Delta\varphi_{RF} + \Delta\varphi_{RF}^{dem})|^2 S_{AOM} \quad (14)$$

where the white noise components S_0^{op} and S_0^{RF} of Eqs. (13) and (14), are the minimum values of the measured curves S_{out}^{op} and S_{out}^{RF} , while the dephasings added from the demodulation schemes are modeled by the following expressions:

$$\Delta\varphi_{RF}^{dem}(f) = \arctan(f/f_{RF}^{dem}) \quad (15)$$

$$\Delta\varphi_{op}^{dem}(f) = \arctan(f/f_{op}^{dem}) \quad (16)$$

The fit results (purple and cyan dashed lines) are plotted against the data in Fig. 4. We obtain the following characteristic frequencies: $f_{RF}^{dem} = 0.416(1)$ MHz and $f_{op}^{dem} = 5.00(3)$ MHz.

Regarding the white noise minima, we obtain $S_0^{RF} = 4.30(1) \times 10^{-13}$ rad²/Hz and $S_0^{op} = 1.00(1) \times 10^{-12}$ rad²/Hz.

We observe that S_0^{RF} is almost 10 times greater than the expected detection noise S_{det} calculated by using Eq. (9). This discrepancy can be easily explained by considering an underestimation of the photodiode amplifier noise figure and excess noise coming from the environment at frequencies below 10 kHz.

Finally, we demonstrate the noise improvement of the CRNI. To further evince the relative sensitivity of the considered demodulation schemes, we define G as the ratio of the measured phase noise $G = S_{out}^{RF}/S_{out}^{op}$. The factor G obtained from the measured spectra in Fig. 4 is reported in Fig. 5 (green curve), and compared with the ratio between the expected interferometric noises $G^{est} = S_{int}^{RF}/S_{int}^{op}$ (orange curve). At frequencies above 50 kHz, the optical demodulation shows a noise improvement compared to the RF demodulation, surpassing 3 dB in the frequency interval 100–900 kHz. At frequencies below 50 kHz, optical demodulation offers a sensitivity that goes 3 dB lower compared to RF demodulation.

5. Discussion

We now discuss the significance and the implications of the results found in the previous section.

In Fig. 5 we have demonstrated a noise improvement of the CRNI compared to the standard interferometric methods based on RF demodulation above 50 kHz. We attribute this high-frequency noise improvement to the higher bandwidth of common mode noise rejection.

In fact, in the RF demodulation scheme, the characteristic delay time is set by the AOM rise time τ_r . This is the typical time for the acoustic wave to pass through the optical beam, and therefore it defines the minimum time required for the optical beam to respond to a change in the RF signal. The AOM rise time is estimated as $\tau_r \simeq w/v_s = 290(50)$ ns where $w = 1.2(2)$ mm is the optical beam diameter and $v_s =$

4.2 km s⁻¹ is used. The rising time τ_r provides a bandwidth response of $(2\pi\tau_r)^{-1} = 0.54(9)$ MHz which is in agreement with the fit value f_{RF}^{dem} found in Eq. (15) within 2σ . On the other hand, in the optical demodulation scheme, the measured characteristic frequency $f_{op}^{dem} = 5.00(3)$ MHz results in a delay time $\tau_{op}^{dem} = (2\pi f_{op}^{dem})^{-1} = 31.8(2)$ ns, which is much shorter than τ_r . In the CRNI, both optical branches are affected by the AOM rising time and so they are perfectly time compensated after the demodulation process, providing an high degree of common mode RF noise rejection.

Several possible physical effects could determine the CRNI delay time τ_{op}^{dem} . One source of delay time in an optical interferometer is associated with the unbalanced optical path lengths of the branches. In our system we estimate a maximum branches' unbalance $\Delta l \leq 20$ cm would generate an optical time delay $\tau_o = \Delta l/c \simeq 0.66$ ns, or a frequency cut-off of 240 MHz. This exceeds all other cut-off frequencies measured and the phasemeter measurement bandwidth. Another technical source of delay may be caused by different lengths of the RF cables that reach the mixers. However, if we consider RG58 cables whose electric field propagation speed is almost $(2/3)c$, the necessary RF cable length difference is about 6.4 m, while we use the same cable length to connect both photodiodes to the RF chain depicted in Fig. 3. Finally, the non-pure RN diffraction regime ($Q \simeq 1$) generating our CRNI could be the source of both a small amplitude imbalance, and a relative phase shift among the diffracted components, as previously observed [21]. This could in principle explain the presence of the measured characteristic time among the branches of the interferometer. If this is the case, one would expect that τ_{op}^{dem} can be reduced when working at a lower modulation frequency or with a thinner Bragg cell designed to achieve a pure Raman-Nath regime [21]. This uncompensated residual time τ_{op}^{dem} prevents us from fully reaching the ultimate limit of the interferometer shown in the black curve of Fig. 4.

After discussing the performance of our CRNI prototype at high Fourier frequencies, we analyze its low-frequency performance.

At low frequencies, where S_{env} dominates the noise spectrum, the CRNI is limited by the redundancy of the optical setup, and a factor of 2 higher noise is expected, as shown in Eq. (7). Indeed, the CRNI estimated white noise level S_0^{op} is 2.32(5) times higher than S_0^{RF} , in agreement with the redundancy hypothesis. Moreover, similar results would be expected if we were limited by the shot noise from the detectors.

Finally, we outline some possible improvements to push the sensitivity of a CRNI and some possible applications.

A possible way to greatly improve the low-frequencies phase noise performances of the CRNI is to carefully design the double interferometer branches in such a way that they share the same optical elements from the separation region where the RN modulation is applied to the detection region where two photodiodes are employed. We expect that this shrewdness will highly suppress the seismic and acoustic noise coupled at low frequency even compared with the RF demodulation

counterpart. The ultimate phase noise limit of this compact composite interferometer is provided by the shot-noise induced by the two photodiodes employed to acquire the beatnotes.

Regarding the applicability of the CRNI method, it has been already employed as a simple system to measure the phase noise of an actuator under test without introducing a duplicate system, as reported in [18]. The frequency bandwidth where our interferometer demonstrates noise improvement could be particularly valuable for fiber optic undersea applications, especially in military sonar and seismic surveying [34,35].

6. Conclusions

In this work, we theoretically and experimentally studied in detail a composite heterodyne interferometer which exploits the Raman-Nath regime of the AOM. We discussed the limits of the CRNI by quantitatively comparing the optical demodulation scheme with the RF counterpart. We introduced a theoretical model which can be easily adapted to figure out the typical phase noise performance of an optical heterodyne interferometer. Employing the CRNI to measure the phase noise of a test frequency shifter, we measure a noise improvement in the 50 kHz–1 MHz range, reaching 4 dB at 300 kHz. This sensitivity enhancement lays within a frequency band of particular interest in precise optical spectroscopy in the framework of quantum logic spectroscopy and quantum information. In particular, frequency-stabilized diode lasers experience an excess of phase noise in this bandwidth [9]. As suggested by [22], we believe that our interferometer is an experimental alternative for implementing real-time protocols for quantum non-demolition experiment [36,37].

CRedit authorship contribution statement

Matteo Barbiero: Writing – review & editing, Writing – original draft, Visualization, Investigation. **Juan Pablo Salvatierra:** Writing – review & editing, Investigation. **Daide Calonico:** Writing – review & editing, Supervision. **Filippo Levi:** Writing – review & editing, Supervision. **Marco G. Tarallo:** Writing – review & editing, Writing – original draft, Supervision.

Declaration of competing interest

The authors declare that they have no known competing financial interests or personal relationships that could have appeared to influence the work reported in this paper.

Data availability

Data will be made available on request.

Acknowledgments

We thank C. Clivati and C. Calosso for fruitful discussions, M. Gozzelino for lending the phasemeter, and H. Cook for proofreading the manuscript.

References

- [1] D. Bluvstein, S.J. Evered, A.A. Geim, S.H. Li, H. Zhou, T. Manovitz, S. Ebad, M. Cain, M. Kalinowski, D. Hangleiter, J.P.B. Ataiades, N. Maskara, I. Cong, X. Gao, P.S. Rodriguez, T. Karolyshyn, G. Semeghini, M.J. Gullans, M. Greiner, V. Vuletić, M.D. Lukin, Logical quantum processor based on reconfigurable atom arrays, *Nature* (2023) <http://dx.doi.org/10.1038/s41586-023-06927-3>.
- [2] J.P. Covey, H. Weinfurter, H. Bernien, Quantum networks with neutral atom processing nodes, *NPJ Quantum Inf.* 9 (1) (2023) <http://dx.doi.org/10.1038/s41534-023-00759-9>.
- [3] C.D. Bruzewicz, J. Chiaverini, R. McConnell, J.M. Sage, Trapped-ion quantum computing: Progress and challenges, *Appl. Phys. Rev.* 6 (2) (2019) <http://dx.doi.org/10.1063/1.5088164>.
- [4] A.M. Kaufman, K.-K. Ni, Quantum science with optical tweezer arrays of ultracold atoms and molecules, *Nat. Phys.* 17 (12) (2021) 1324–1333, <http://dx.doi.org/10.1038/s41567-021-01357-2>.
- [5] C. Hempel, C. Maier, J. Romero, J. McClean, T. Monz, H. Shen, P. Jurcevic, B.P. Lanyon, P. Love, R. Babbush, A. Aspuru-Guzik, R. Blatt, C.F. Roos, Quantum chemistry calculations on a trapped-ion quantum simulator, *Phys. Rev. X* 8 (3) (2018) <http://dx.doi.org/10.1103/physrevx.8.031022>.
- [6] H. Bernien, S. Schwartz, A. Keesling, H. Levine, A. Omran, H. Pichler, S. Choi, A.S. Zibrov, M. Endres, M. Greiner, V. Vuletić, M.D. Lukin, Probing many-body dynamics on a 51-atom quantum simulator, *Nature* 551 (7682) (2017) 579–584, <http://dx.doi.org/10.1038/nature24622>.
- [7] M. Schulte, C. Lisdat, P.O. Schmidt, U. Sterr, K. Hammerer, Prospects and challenges for squeezing-enhanced optical atomic clocks, *Nature Commun.* 11 (1) (2020) <http://dx.doi.org/10.1038/s41467-020-19403-7>.
- [8] J.G. Bohnet, B.C. Sawyer, J.W. Britton, M.L. Wall, A.M. Rey, M. Foss-Feig, J.J. Bollinger, Quantum spin dynamics and entanglement generation with hundreds of trapped ions, *Science* 352 (6291) (2016) 1297–1301, <http://dx.doi.org/10.1126/science.aad9958>.
- [9] M.L. Day, P.J. Low, B. White, R. Islam, C. Senko, Limits on atomic qubit control from laser noise, *NPJ Quantum Inf.* 8 (1) (2022) 72, <http://dx.doi.org/10.1038/s41534-022-00586-4>.
- [10] X. Jiang, J. Scott, M. Friesen, M. Saffman, Sensitivity of quantum gate fidelity to laser phase and intensity noise, *Phys. Rev. A* 107 (4) (2023) <http://dx.doi.org/10.1103/physreva.107.042611>.
- [11] J.W. Wagner, J.B. Spicer, Theoretical noise-limited sensitivity of classical interferometry, *J. Opt. Soc. Am. B* 4 (8) (1987) 1316, <http://dx.doi.org/10.1364/josab.4.001316>.
- [12] A. Buonanno, Y. Chen, N. Mavalvala, Quantum noise in laser-interferometer gravitational-wave detectors with a heterodyne readout scheme, *Phys. Rev. D* 67 (12) (2003) <http://dx.doi.org/10.1103/physrevd.67.122005>.
- [13] J.H. McElroy, Infrared heterodyne solar radiometry, *Appl. Opt.* 11 (7) (1972) 1619, <http://dx.doi.org/10.1364/ao.11.001619>.
- [14] R.G. Frehlich, M.J. Kavaya, Coherent laser radar performance for general atmospheric refractive turbulence, *Appl. Opt.* 30 (36) (1991) 5325, <http://dx.doi.org/10.1364/ao.30.005325>.
- [15] G.C. Bjorklund, M.D. Levenson, W. Lenth, C. Ortiz, Frequency modulation (FM) spectroscopy: Theory of lineshapes and signal-to-noise analysis, *Appl. Phys. B* 32 (3) (1983) 145–152, <http://dx.doi.org/10.1007/bf00688820>.
- [16] Y. He, B. Orr, Rapidly swept, continuous-wave cavity ringdown spectroscopy with optical heterodyne detection: single- and multi-wavelength sensing of gases, *Appl. Phys. B* 75 (2–3) (2002) 267–280, <http://dx.doi.org/10.1007/s00340-002-0983-8>.
- [17] L. Richter, H. Mandelberg, M. Kruger, P. McGrath, Linewidth determination from self-heterodyne measurements with subcoherence delay times, *IEEE J. Quantum Electron.* 22 (11) (1986) 2070–2074, <http://dx.doi.org/10.1109/jqe.1986.1072909>.
- [18] M. Barbiero, J.P. Salvatierra, M. Risaro, C. Clivati, D. Calonico, F. Levi, M.G. Tarallo, Broadband heterodyne phase modulation for optical frequency standards and spectral purity transfer, *Opt. Lett.* 48 (7) (2023) 1958, <http://dx.doi.org/10.1364/ol.485064>.
- [19] F. Zernike, A precision method for measuring small phase differences, *J. Opt. Soc. Am.* 40 (5) (1950) 326–328, <http://dx.doi.org/10.1364/JOSA.40.000326>, URL <https://opg.optica.org/abstract.cfm?URI=josa-40-5-326>.
- [20] V. Baryshev, V. Epikhin, L. Kopylov, Y. Domnin, FM spectroscopy of CPT resonances with AOM operating purely in the Raman-Nath diffraction regime as optic phase modulator, in: 2009 IEEE International Frequency Control Symposium Joint with the 22nd European Frequency and Time Forum, IEEE, 2009, pp. 582–586, <http://dx.doi.org/10.1109/freq.2009.5168249>.
- [21] V.N. Baryshev, V.M. Epikhin, Compact acousto-optic modulator operating in the purely Raman-Nath diffraction regime as a phase modulator in FM spectroscopy, *Quantum Electron.* 40 (5) (2010) 431–436, <http://dx.doi.org/10.1070/qe2010v04n05abeh014074>.
- [22] J.-B. Béguin, E. Bookjans, S. Christensen, H. Sørensen, J. Müller, E. Polzik, J. Appel, Generation and detection of a sub-Poissonian atom number distribution in a one-dimensional optical lattice, *Phys. Rev. Lett.* 113 (26) (2014) <http://dx.doi.org/10.1103/physrevlett.113.263603>.
- [23] S. Cook, T. Rosenband, D.R. Leibbrandt, Laser-frequency stabilization based on steady-state spectral-hole burning $\text{Eu}^{3+}:\text{Y}_2\text{SiO}_5$, *Phys. Rev. Lett.* 114 (25) (2015) <http://dx.doi.org/10.1103/physrevlett.114.253902>.
- [24] N. Galland, N. Lučić, S. Zhang, H. Alvarez-Martinez, R.L. Targat, A. Ferrier, P. Goldner, B. Fang, S. Seidelin, Y.L. Coq, Double-heterodyne probing for an ultra-stable laser based on spectral hole burning in a rare-earth-doped crystal, *Opt. Lett.* 45 (7) (2020) 1930, <http://dx.doi.org/10.1364/ol.389833>.
- [25] E. Rubiola, E. Salik, S. Huang, N. Yu, L. Maleki, Photonic-delay technique for phase-noise measurement of microwave oscillators, *J. Opt. Soc. Am. B* 22 (5) (2005) 987, <http://dx.doi.org/10.1364/josab.22.000987>.
- [26] W. Klein, B. Cook, Unified approach to ultrasonic light diffraction, *IEEE Trans. Sonics Ultrason.* 14 (3) (1967) 123–134, <http://dx.doi.org/10.1109/t-su.1967.294223>.

- [27] I. Chang, *Acousto-Optic Devices and Applications in Handbook of Optics*, second ed., McGraw-Hill Professional, New York, NY, 1994.
- [28] D. Kedar, Z. Yao, I. Ryger, J.L. Hall, J. Ye, Synthetic FM triplet for AM-free precision laser stabilization and spectroscopy, 2023, [arXiv:arXiv:2311.14268](https://arxiv.org/abs/2311.14268).
- [29] C.W.C. Weng, X.Z.X. Zhang, Model of Raman-Nath acousto-optic diffraction, *Chin. Opt. Lett.* 13 (10) (2015) 101701–101705, <http://dx.doi.org/10.3788/col201513.101701>.
- [30] V. Baryshev, E. Aleinikova, Residual amplitude modulation and birefringence effects in EOM and AOM-RN, in: 2014 European Frequency and Time Forum, EFTF, IEEE, 2014, pp. 525–527, <http://dx.doi.org/10.1109/efrf.2014.7331553>.
- [31] C.A. Barnes, A. Hati, C.W. Nelson, D.A. Howe, Residual PM noise evaluation of radio frequency mixers, in: 2011 Joint Conference of the IEEE International Frequency Control and the European Frequency and Time Forum (FCS) Proceedings, 2011, pp. 1–5, <http://dx.doi.org/10.1109/FCS.2011.5977868>.
- [32] Mini-Circuits, Additive phase noise in amplifier, 2021, <https://blog.minicircuits.com/additive-phase-noise-in-amplifiers/>.
- [33] J.P. Salvatierra, Optical Frequency Stabilization to a Doubly Forbidden Atomic Transition for a Strontium Optical Lattice Clock (Master's thesis), Università di Torino, 2022.
- [34] R.D. Paula, J. Cole, J. Bucaro, Broad-band ultrasonic sensor based on induced optical phase shifts in single-mode fibers, *J. Lightwave Technol.* 1 (2) (1983) 390–393, <http://dx.doi.org/10.1109/jlt.1983.1072126>.
- [35] G.A. Cranch, R. Crickmore, C.K. Kirkendall, A. Bautista, K. Daley, S. Motley, J. Salzano, J. Latchem, P.J. Nash, Acoustic performance of a large-aperture, seabed, fiber-optic hydrophone array, *J. Acoust. Soc. Am.* 115 (6) (2004) 2848–2858, <http://dx.doi.org/10.1121/1.1710504>.
- [36] M.G. Tarallo, Toward a quantum-enhanced strontium optical lattice clock at INRIM, in: E. Puppini (Ed.), EPJ Web Conf. 230 (2020) 00011, <http://dx.doi.org/10.1051/epjconf/202023000011>.
- [37] A. Caprotti, M. Barbiero, M.G. Tarallo, M.G. Genoni, G. Bertaina, Analysis of spin-squeezing generation in cavity-coupled atomic ensembles with continuous measurements, *Quantum Sci. Technol.* 9 (3) (2024) 035032, <http://dx.doi.org/10.1088/2058-9565/ad4584>.